scientific reports

Check for updates

OPEN

Experimental study and model prediction of the influence of different factors on the mechanical properties of saline clay

Hui Cheng, Lingkai Zhang✉, Chong Shi & Pei Pei Fan

Water conveyance channels in cold and arid regions pass through several saline-alkali soil areas. Canal water leakage exacerbates the salt expansion traits of such soil, damaging canal slope lining structures. To investigate the mechanical properties of saline clay, this study conducted indoor tests, including direct shear, compression, and permeation tests, and scanning electron microscopy (SEM) analysis of soil samples from typical sites. This study aims to elucidate the impact of various factors on the mechanical properties of saline clay from a macro–micro perspective and reveal its physical mechanisms. A prediction model is formulated and validated. The findings indicate the following: (1) Cohesion in direct shear tests has a linear negative correlation with water content and a positive correlation with dry density and initially decreases with increasing salt content until 2%, after which it increases. The internal friction angle initially increases and then decreases with increasing water content, reaching a peak at the optimal water content, and then gradually increases with dry density while initially decreasing, followed by an increase in salt content, stabilizing thereafter. Water content, dry density, or salt content chiefly affect cohesion by influencing electrostatic attraction, van der Waals forces, particle cementation, and valence bonds at particle contact points. (2) Compression tests reveal a linear positive correlation between the compression coefficient and water content, a negative correlation with dry density, and a stepwise linear correlation with salt content, peaking at 2%. The compression index decreases with increasing water content and dry density, following a trend similar to that of the compression coefficient with increasing salt content. The rebound index shows a linear negative correlation with water content and dry density, transitioning from a negative to a positive correlation at 2% salt content. Scanning electron microscopy analysis revealed particle flattening and increased aggregation with increasing consolidation pressure, reducing compressibility. Large pores and three-dimensional porosity have the greatest influence on soil compressibility. (3) Permeability tests reveal an exponential negative correlation between the permeability coefficient and dry density. As the dry density increases, the particle arrangement becomes denser, decreasing the pore quantity, with micropores disproportionately impacting the permeability coefficient. An increase in salinity initially increases the permeability coefficient before it decreases. The boundary point of the 2% salt content divides the effect of salt ions from promoting free water flow to blocking seepage channels, with the proportion of micropores being the primary influencing factor. (4) Employing statistical theory and machine learning algorithms, dry density, water content, and salinity are used to predict mechanical index values. The improved particle swarm optimization-support vector regression (PSO-SVR) model has high accuracy and general applicability. These findings offer insights for the construction and upkeep of open channel projects in arid regions.

In the cold and arid areas of Northwest China, the degradation of canal foundation soil is the fundamental cause of canal foundation damage[1]. For example, the first phase of the water supply project in northern Xinjiang, which crosses cold deserts, gobi deserts, and sand deserts in northwestern China, was a large-scale water transfer

College of Hydraulic and Civil Engineering, Xinjiang Agricultural University, 311 East Nongda Rd, Urumqi 830052, China. ✉email: xjauzhanglk@163.com

project with long distances, large flows, and inter-basin transfers. Its plain canal section is 57.23 km long, with a shallow burial depth of groundwater and a high content of SO_4^{2-} ions in water, resulting in severe salt frost heave and obvious degradation of the canal foundation soil.

At present, numerous studies have been carried out on the salt heave characteristics and mechanisms of sulfate-salinized soils, yielding interim findings through the integration of frozen soil research[2–4]. This work establishes a foundation for further examination of the engineering properties of these soils. In the context of the mechanical properties of silty clay, prevailing research predominantly examines the effects of various factors on the mechanical properties of cohesive soil via routine laboratory tests. Specifically, (1) for direct shear tests, various scholars have implemented direct shear tests under different conditions, such as moisture content, dry density, and particle size distribution, to assess the effects on the mechanical properties of cohesive soils. It has been observed that increased water content reduces soil strength and significantly influences the shear strength parameters of soil displacement[5–7]. Conversely, as the dry density increases, so does the shear strength of the soil[8], with the particle size distribution being a critical factor in determining the shear strength of the soil[9].

(2) Regarding compression tests, research has indicated that the combined effects of moisture content, salinity, and temperature primarily cause soil settlement[10]. Recent studies have demonstrated through compression tests under varying conditions that the moisture content, dry density[11], and overlying pressure[12–14] significantly affect the compression characteristics of silty clay, with the remolded yield stress decreasing as the initial moisture content increases. (3) In permeation test research, Wu[15], Zarooei[16], Mohammed and Mahmood[17] explored the effects of varying compaction degrees and particle size distributions on the permeability coefficient under different water head permeation tests and reported that increased compaction reduces the permeability coefficient, which is closely linked to the grain size distribution index of the soil body. Furthermore, Hu[18] compared the permeability results obtained from the Gardner model with those of two other commonly utilized methods (the constant head method and van Genuchten model). (4) Concerning microstructure: Current research often involves the use of scanning electron microscopy (SEM) to qualitatively and quantitatively analyze changes in microstructure under various conditions[19]. Additionally, mercury intrusion porosimetry experiments have allowed scholars to quantitatively assess changes in the pore structure of silty clay, which are pivotal in influencing its mechanical properties. Moreover, techniques such as nuclear magnetic resonance (NMR)[20–22] and computed tomography (CT)[23,24] are increasingly used to study the microstructure of cohesive soils, with CT imaging frequently employed to create three-dimensional pore structures.

On the other hand, by utilizing methods such as statistics[25], data mining[26], and machine learning[27] to analyze the relationships between the strength and deformation of silty clay and various factors, a predictable model for silty clay strength parameters has been developed. This is highly important for understanding and predicting changes in silty clay strength. Most existing prediction models require extensive sample data for support. However, in actual engineering applications, the amount of test and inspection data available is relatively small, which makes it impossible to quickly and accurately judge the changes in the mechanical properties of saline clay. Among these, the support vector machine (SVM) predictive modeling technique possesses a notable advantage in small sample data. Furthermore, SVMs are better suited to solving problems with small samples and nonlinearities, as they have superior generalizability capabilities[28].

Research on sulfate saline-alkali soil and silty clay has revealed several notable characteristics. First, it covers a wide range of topics, including salt heave characteristics, mechanical properties, compression behavior, permeability, and microstructure. Second, various experimental methods, such as direct shear tests, compression tests, permeability tests, and scanning electron microscope experiments, are employed to provide comprehensive insights. However, there are also several limitations. For example, while many studies have focused on individual factors, comprehensive research on the interactions among multiple factors is lacking. Additionally, further validation and refinement of the mathematical models used to simulate soil behavior are needed. Furthermore, more research is needed to understand the long-term impact of sulfate saline-alkali soil on engineering structures and to develop effective mitigation strategies. Therefore, this paper aims to investigate the impact of various factors on the basic mechanical properties of saline clay at the macroscopic level through direct shear, compression, permeability, and scanning electron microscopy (SEM) tests conducted on saline clay from a major canal in the north. Furthermore, this work aims to elucidate the deterioration mechanism of its physical properties at the microscopic level. Taking water content, dry density, and salt content as characteristic variables, this paper establishes a prediction model for the strength parameters of saline soil, which can provide a reference for the safe operation and maintenance of water conveyance canals in cold and arid regions.

Materials and methods
Test materials
The soil samples used in the test were taken from a water conveyance open channel project in northern China and were composed of silty clay. The basic physical properties of the soil samples were measured according to the "Standard for Soil Test Methods" (GB/T50123-2019). The basic physical properties and particle size distributions of the soil samples are presented in Table 1 and Fig. 1a, respectively. From Fig. 1a, it is evident that the clay soil falls within the category of low-liquid-limit clay (CL) with poor grading. The soluble salt content, mineral

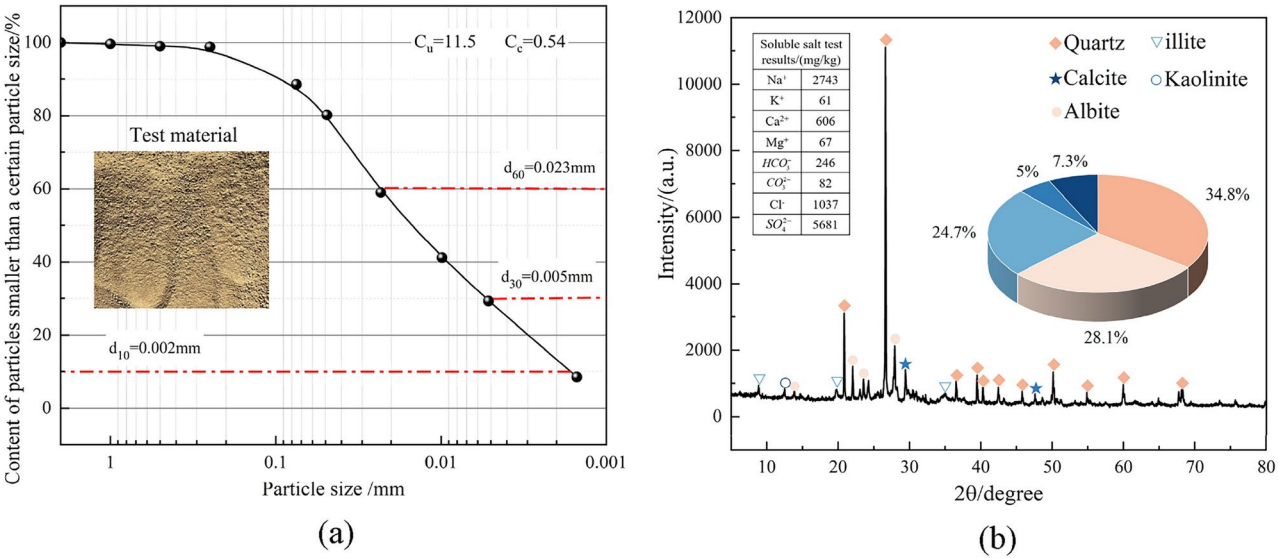| Optimum water content $w_{0p}/\%$	Max. dry density $\rho_{dmax}/g\,cm^{-3}$	Specific gravity G_s	Liquid limit $W_L/\%$	Plastic limit $W_p/\%$
17.3	1.77	2.68	31.4	14.09

Table 1. Basic physical indicators.

Fig. 1. Basic physical properties of the specimens: (**a**) particle grading curve and (**b**) X-ray diffraction results.

Different water contents			Different dry densities			Different salt contents		
Water contents w/%	Dry density ρ_d/g·cm^{-3}	Salt contents s/%	Water contents w/%	Dry density ρ_d/g·cm^{-3}	Salt contents s/%	Water contents w/%	Dry density ρ_d/g·cm^{-3}	Salt contents s/%
15.3	1.68	0.5	17.3	1.50 1.59 1.68 1.77	0.5	17.3	1.68	0
17.3								1
19.3								2
21.3								3
								4
								5

Table 2. Direct shear test and compression test schemes.

Different dry densities			Different salt contents		
Water contents w/%	Dry density ρ_d/g·cm^{-3}	Salt contents s/%	Water contents w/%	Dry density ρ_d/g·cm^{-3}	Salt contents s/%
17.3	1.52	0.5	17.3	1.68	0
	1.57				1
	1.62				2
	1.67				3
	1.72				4
	1.77				5

Table 3. Penetration test scheme.

composition, and X-ray diffraction (XRD) results are depicted in Fig. 1b. As per the "Code for Investigation of Geotechnical Engineering" (GB 50021-2001), a sodium ion content of 0.568% is classified as medium saline soil. The primary mineral components of the soil samples include quartz, albite, and calcite, among others.

Test methods

All the soil samples used in this experiment were remolded. The specific experimental design indicators are shown in Tables 2 and 3. The design indicators for the dry density and moisture content of the clayey soil are below the compaction test curve, and the required design indicators for the clayey soil can be obtained through compaction. The specific procedures for sample preparation were as follows: (1) After naturally air-drying the collected soil samples, they were crushed and sieved through a 2 mm diameter sieve. The sieved soil samples were then washed to remove salt until the conductivity coefficient of the elution solution no longer changed, indicating that the salt washing was complete. (2) The salt-washed soil samples were placed in an oven at 105 °C
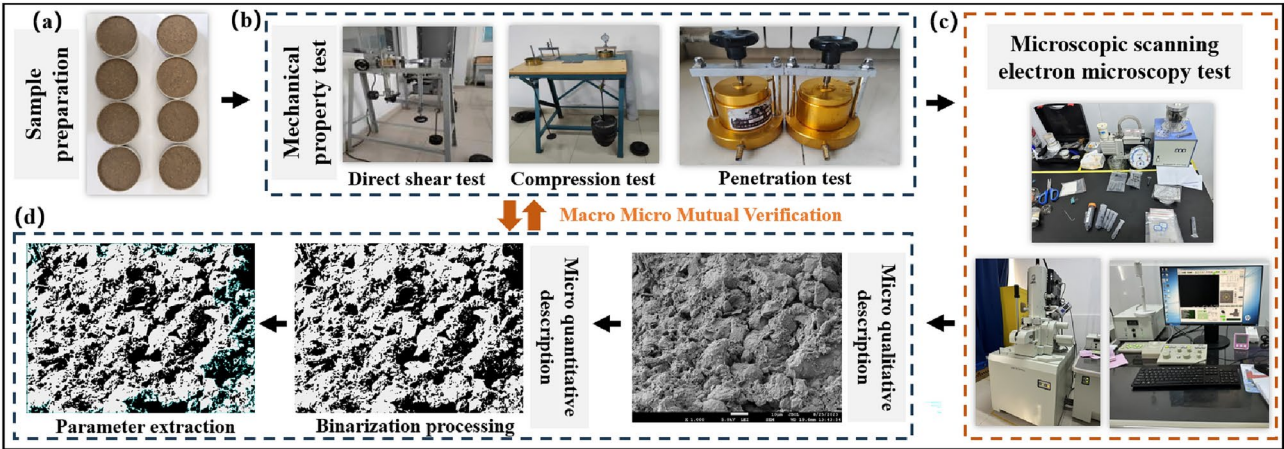
Fig. 2. Schematic diagram of the test process: (**a**) specimen preparation; (**b**) instruments used for the direct shear test, compression test, and penetration test; (**c**) gold spraying treatment and SEM test; (**d**) qualitative and quantitative analysis of microstructural changes using SEM images.

Microscopic parameters	Pore proportion	V_{3D}	Abundance	Roundness	Directional frequency
Computing formula	$P = \frac{A_c}{A} \times 100\%$	$V_{3D} = \sum_{i=1}^{N} \frac{S_i(255 - D_i)}{255N}$	$C = \frac{B}{L}$	$R = \frac{4\pi s}{p^2}$	$F(\alpha) = \frac{n_\alpha}{n}$

Table 4. Quantitative parameter calculation formula for the microstructure. P represents the porosity, A_c represents the area of each pore, A represents the total area of the pores, s represents the particle area, p represents the perimeter of the particles, S represents the area of each pixel, and we select the unit pixel as the benchmark. N represents the total number of pixels, S_i represents the area of each pixel, and D_i represents the gray value corresponding to the ith pixel; B and L represent the lengths of the short and long axes, respectively; α represents the angle between the pore or particle and the horizontal direction; $F_i(\alpha)$ represents the orientational frequency; n_α represents the number of pores or particles within each orientational interval; and n represents the total number of pores or particles.

for 24 h to dry them. The dried soil samples were then weighed according to the set moisture content and dry density and mixed with sodium sulfate salt solutions with mass fractions of 0% (distilled water), 0.5%, 1%, 2%, 3%, 4%, and 5%. Under constant-temperature conditions, dry soil and salt solution were mixed uniformly and placed in a plastic bag for 24 h to ensure a uniform distribution of moisture and salt. (3) Ring knife samples were prepared from the prepared soil samples according to the experimental scheme.

In line with the experimental plan, sample preparation was conducted as illustrated in Fig. 2a. Direct shear, compression, and permeability tests were subsequently performed, as depicted in Fig. 2b. Micro-scanning was conducted on soil samples with varying dry densities, initial salt contents, and consolidation pressures, as well as on samples subjected to post-permeability tests with different dry densities and salt contents (Fig. 2c). SEM images were captured to qualitatively describe the microstructural changes. Uniform processing of images at 4000× and 10,000× magnifications was carried out via ImageJ software, and relevant micro-parameters were extracted for quantitative analysis (Fig. 2d). The formulas for calculating the micro-quantitative parameters are delineated in Table 4.

Results and analysis
Direct shear test
Macroscopic analysis
Figure 3 shows the curves of the influence of different water contents, dry densities, and salt contents on the shear index of saline clay. (1) Figure 3a shows the influence curve of different water contents on the shear strength of saline clay. Figure 3a shows that the cohesion decreases linearly with increasing water content; the internal friction angle is less affected by the water content, the overall change trend first increases and then decreases, and the optimal water content is the turning point. (2) Figure 3b shows the influence curve of dry density on the shear strength of saline clay. Figure 3b shows that under the same water content and salt conditions, the cohesion of saline clay increases linearly with increasing dry density, and the cohesion of the maximum dry density is 1.72 times greater than that of the minimum dry density. The internal friction angle shows a small upward trend with increasing dry density, which is only 0.62°. (3) Figure 3c shows the influence curve of different salt contents on the shear strength of saline clay. Figure 3c shows that $s = 2\%$ is the lowest point of cohesion and the lowest internal friction angle. The cohesion decreases linearly from $s = 0\%$ to $s = 2\%$ by 7.72 kPa, and the internal friction
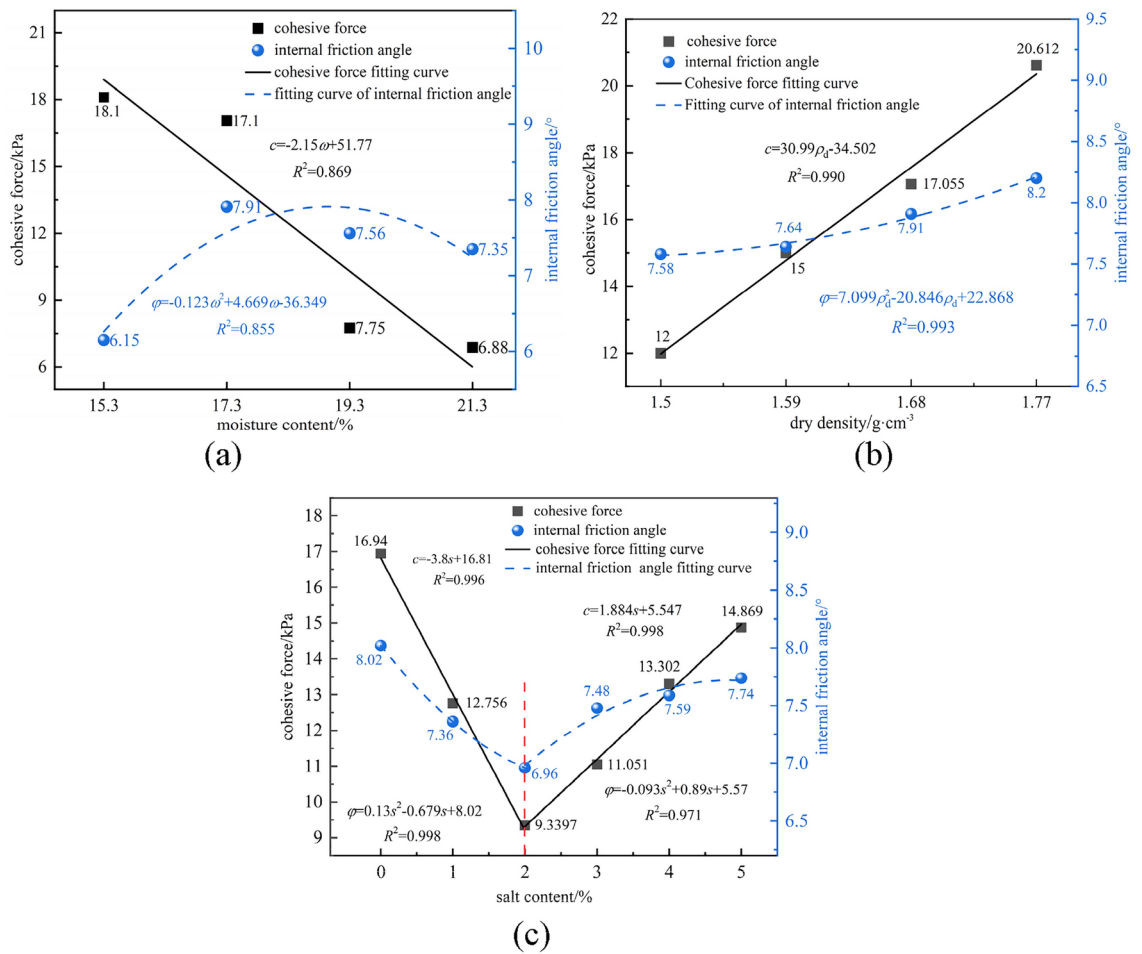
Fig. 3. Influence curves of different factors on the c and φ of cohesive soil: (**a**) different water contents; (**b**) different dry densities; (**c**) different salt contents.

	Correlation	Total number of pores	V_{3D}	Average particle abundance	Particle orientation frequency
ρ_d	a_v	− 0.994**	0.991**	0.699	0.436
	C_c	− 0.960	0.942	0.622	0.597
s	a_v	0.628	0.975**	0.546	0.633
	C_c	0.639	0.945	0.375	0.588

Table 5. Correlations between the compressibility coefficient and microscopic parameters. *$p < 0.05$ **$p < 0.01$.

angle decreases by 0.95°. During the rising stage, from $s = 2\%$ to $s = 5\%$, the cohesion increases by 5.53 kPa, and the internal friction angle increases by 0.78°. These changes are small and gradually tend to stabilize. The fitting parameters are presented in Table 5.

Using JMP statistical analysis software, we employed the least squares method to perform polynomial fitting of three input variables from zero-order to third-order, aiming to establish a mathematical model between the output variable and the input variables.

$$c = -0.096 * (s - 1.35714)^3 + 1594.876 * (\rho_d - 1.667)^3 + 0.253 * (w - 17.586)^3 + 1.33 * (s - 1.357)^2 \\ + 217.578 * (\rho_d - 1.667)^2 - 0.438 * (w - 17.586)^2 - 2.745 * s + 11.874 * \rho_d - 3.914 * w + 63.638 \tag{1}$$

$$\varphi = -0.036 * (s - 1.357)^3 + 79.053 * (\rho_d - 1.667)^3 + 0.036 * (w - 17.586)^3 + 0.241 * (s - 1.357)^2 \\ + 20.234 * (\rho_d - 1.667)^2 - 0.188 * (w - 17.586)^2 - 0.278 * s + 1.911 * \rho_d + 0.093 * w + 2.861 \tag{2}$$

After the initial fitting function was obtained, to verify the accuracy and reliability of the model, the root mean square error (RMSE) between the actual data values and the fitted output values predicted by the model was
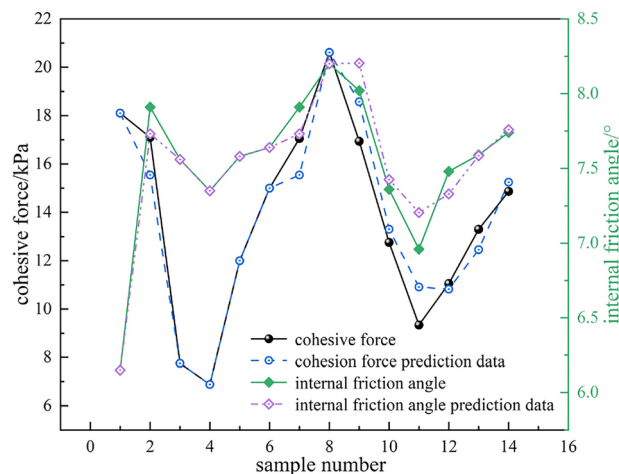
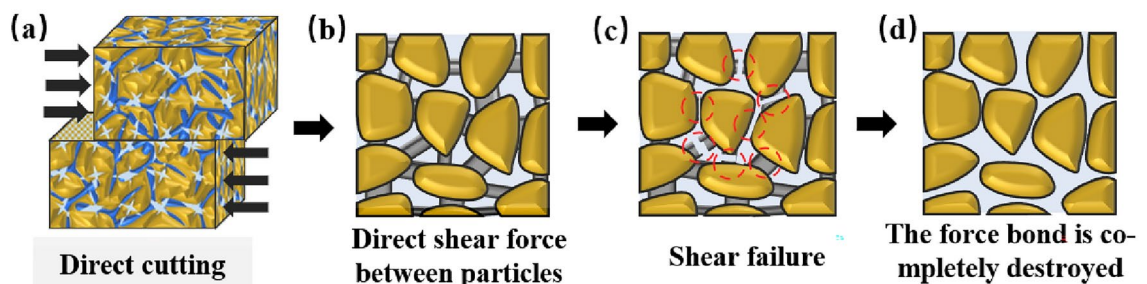**Fig. 4**. Comparison of Experimental and Predicted Values of Shear Strength Parameters.

Fig. 5. Mechanistic diagram of the shear test: (**a**) shearing process; (**b**) interacting forces between particles; (**c**) interaction force between particles destroyed by slope shear action; (**d**) completed shear.

further calculated using MATLAB software. A smaller RMSE value indicates higher prediction accuracy and better fitting performance of the model.

As shown in Fig. 4, the comparison between the actual data values and the fitted output values clearly demonstrates the predictive ability of the model. By comparing the actual data values with the fitted output values, we obtain RMSE values of 0.5913 and 0.0733, respectively, indicating that the established model has high prediction accuracy and good fitting effects. This result provides a solid foundation for subsequent research and applications.

Shear mechanism analysis
Figure 5 shows a schematic diagram of the shear test mechanism. As shown in Fig. 5, the shear action mainly destroys the cementation force between particles.

(1) The moisture content has a significant effect on cohesion. As the water content increases, cohesion decreases. This occurs because as the water content increases, the distance between particles increases, leading to an increase in the water film thickness and a weakening of connections (Fig. 6). Consequently, the Coulomb force, van der Waals force, and cementation force weaken. At lower moisture contents, particles in saline clay are in a relatively loose state due to the lack of sufficient water, resulting in relatively small friction and interlocking forces between particles. As the moisture content increases, water begins to fill the gaps between particles, forming a lubricating layer that facilitates relative sliding between them. However, this lubricating effect does not immediately lead to a reduction in the internal friction angle, as within a certain range, an increase in moisture content may also enhance the cementation between particles. Therefore, within a certain range of moisture contents, the internal friction angle may increase with increasing moisture content. (2) With increasing dry density, the cohesion increases stably and linearly. The main reason is that as the dry density increases, on the one hand, the spacing between particles gradually decreases, making the solid phase in the soil more compact. This compact structure enhances the interaction forces between soil particles, including the cementation effect of cementitious materials between particles, electrostatic and van der Waals forces between particles, and the bonding effect of bound water. The increase in these forces leads to an increase in cohesion. On the other hand, as the dry density increases, the bound water film between the soil particles becomes more compact and stable, which strengthens the bonding effect of the bound water. With increasing dry density, the contact area between particles in saline clay gradually increases. This increase in contact area results in an increase in the friction
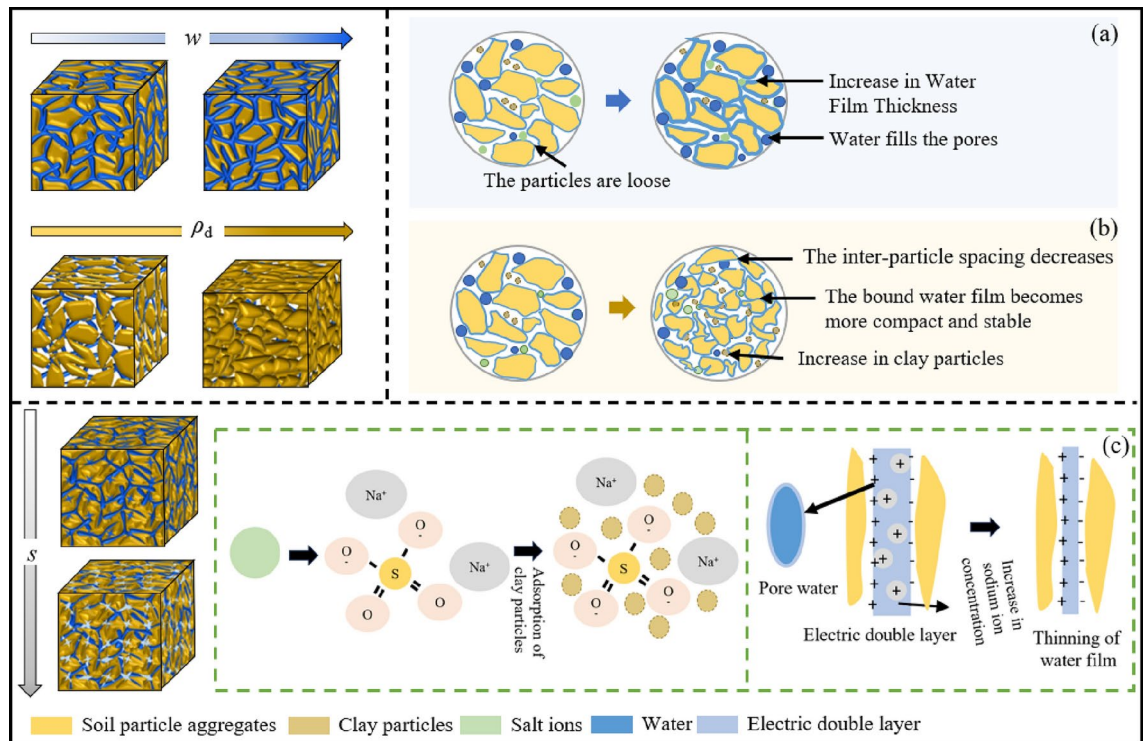
Fig. 6. Diagram illustrating the influence of various factors on particles: (**a**) Changes in particles under the influence of moisture content; (**b**) Changes in particles under the influence of dry density; (**c**) Changes in the bound water film under the influence of salinity.

force between particles, leading to an increase in the internal friction angle. Additionally, as the dry density increases, the particle arrangement may become more compact and orderly. This tight arrangement results in relative movement between particles and more obstacles, thereby increasing the internal friction angle. (3) As the salinity increases, the cohesion of the soil mass undergoes phase changes. The experimental soil sample in this study contained 34.8% quartz and 5% kaolin (Fig. 1b). Quartz is a nonclay mineral with low surface activity and low liquid and plastic limits. The adsorbed bound water film around it is very thin[29,30], resulting in a lack of cohesion between particles. When the salinity increases slightly, more water molecules are adsorbed onto the charged surfaces of soil particles, causing the bound water film between particles to thicken[31], forming a lubricating layer that subsequently reduces the cohesion and friction between particles. However, as the salinity content continues to rise, the contact and packing between particles are gradually replaced by the cementation effect of salt crystals. These salt crystals fill the pores of the soil mass, enhancing its cohesion. Moreover, the cementation effect of salt crystals makes the soil skeleton more compact, and the internal friction angle gradually increases accordingly.

Compression test

Macroscopic result analysis

Figure 7 shows the curves that influence the compression characteristics of saline clay samples with different water contents, dry densities, and salt contents. Figure 7a–c show the e-lg$p$ curves of samples with different water contents, dry densities, and salt contents under different consolidation pressures. Figure 7a–c show that (1) the compression curves of samples under different factors can be divided into three sections, which are initially steep, moderately flat, and straight at the tail. The initial porosity ratios at the different water contents and salt contents are the same. When $s=2\%$, the compression curves of the samples with different salt contents reach the lowest point; the initial porosity ratio gradually decreases with increasing dry density, and the compression curve decreases less. (2) The unloading and reloading rebound segments are regularly affected by the water content, and the differences are basically the same. The higher the water content is, the lower the rebound curve is; the change in the porosity ratio in the rebound segment is obviously affected by the dry density, and the higher the dry density is, the lower the rebound curve is. When $s=2\%$, the rebound curve reaches the lowest point and gradually increases with increasing salt content. Figure 7d–f show the relationship curves of the compression indices of the samples with different water contents, dry densities, and salt contents. Figure 7d shows that with increasing water content, the compression coefficient a_v and the rebound index C_s change in opposite directions, both of which show linear changes, and the fitting parameters are 0.999 and 0.897, respectively; the compression index C_c gradually increases to a stable value with increasing water content. Figure 7e shows that with increasing dry density, the trends of a_v and C_c are the same, both of which decrease linearly, and the fitting degrees are 0.9855 and 0.9355, respectively; C_s shows a linear increasing trend. Figure 6f shows that with increasing salt
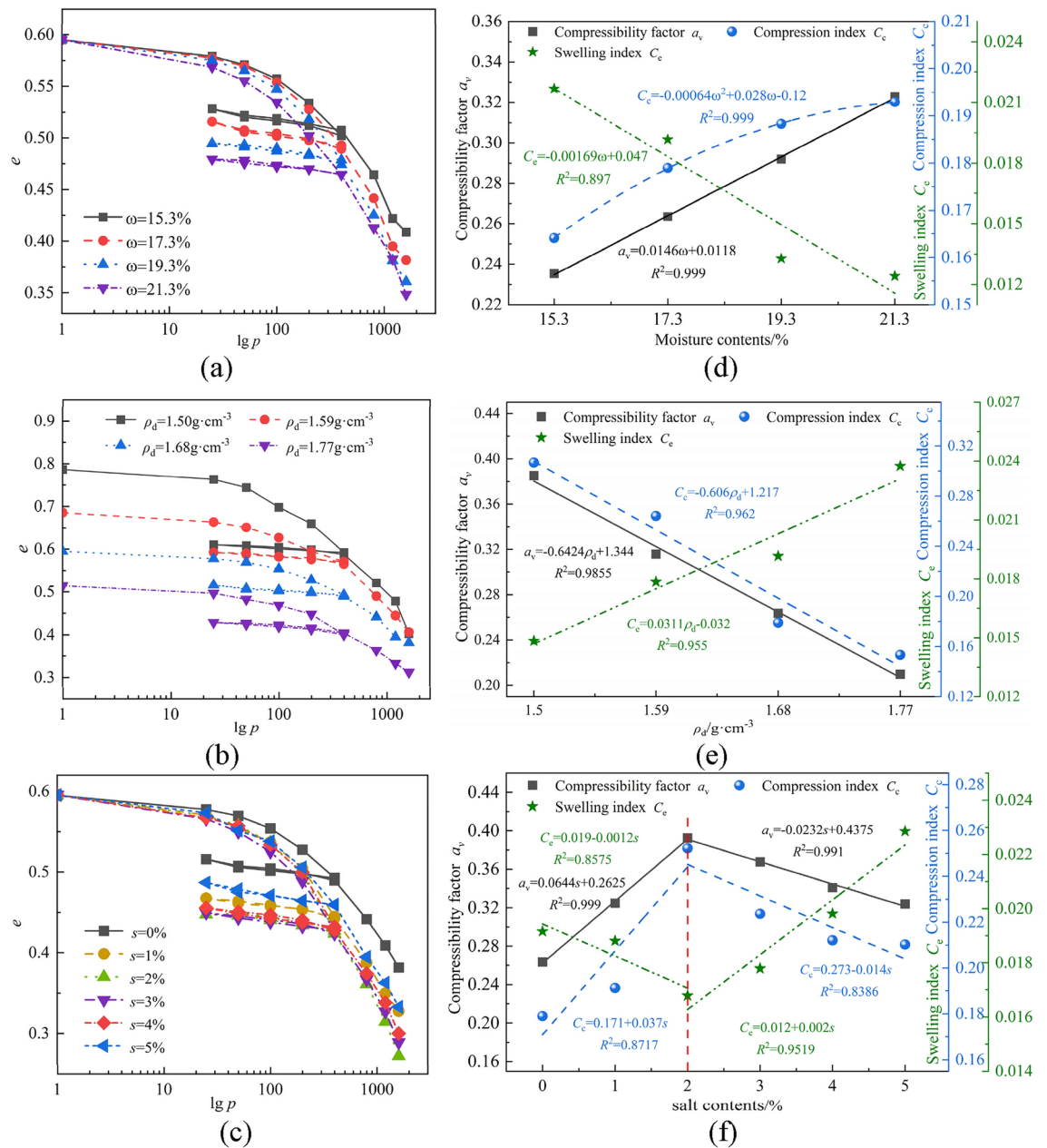
Fig. 7. Effects of different influencing factors on compression indicators: (**a**) e-lg*p* curves under different water contents; (**b**) e-lg*p* curves under different dry densities; (**c**) e-lg*p* curves under different salt contents; (**d**) relationship curves of compression indicators; (**e**) relationship curves of compression indicators; (**f**) relationship curves of compression indicators.

content, a_v and C_c first increase and then decrease, and C_s first decreases and then increases, showing a quadratic function change overall, and the fitting degrees are 0.878, 0.8417, and 0.9355, respectively. A comparison of the experimental and predicted values of the compression coefficient is shown in Fig. 8. The RMSEs are 0.0086, 0.0053 and 1.98E-04.

Microscopic analysis of SEM images under different influencing factors
SEM images of samples with different consolidation pressures and initial samples with different dry densities and salt contents under 4000× magnification were obtained for microanalysis. Figure 9 shows scanning electron microscopy images of samples with different consolidation pressures and initial samples with different dry densities and salt contents.

(1) Figure 9a presents SEM images of the samples under various consolidation pressures. The image reveals that the uncompressed sample has an open flocculation structure with particles distributed directionally yet somewhat dispersed. The soil contains flat clay minerals that form clay mineral aggregates, predominantly
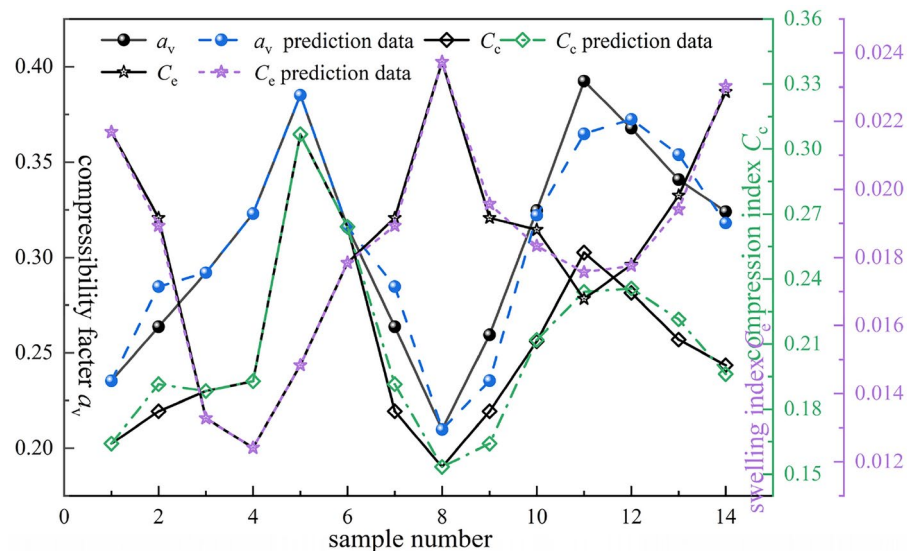
Fig. 8. Comparison of Experimental and Predicted Values of Compression Coefficient.
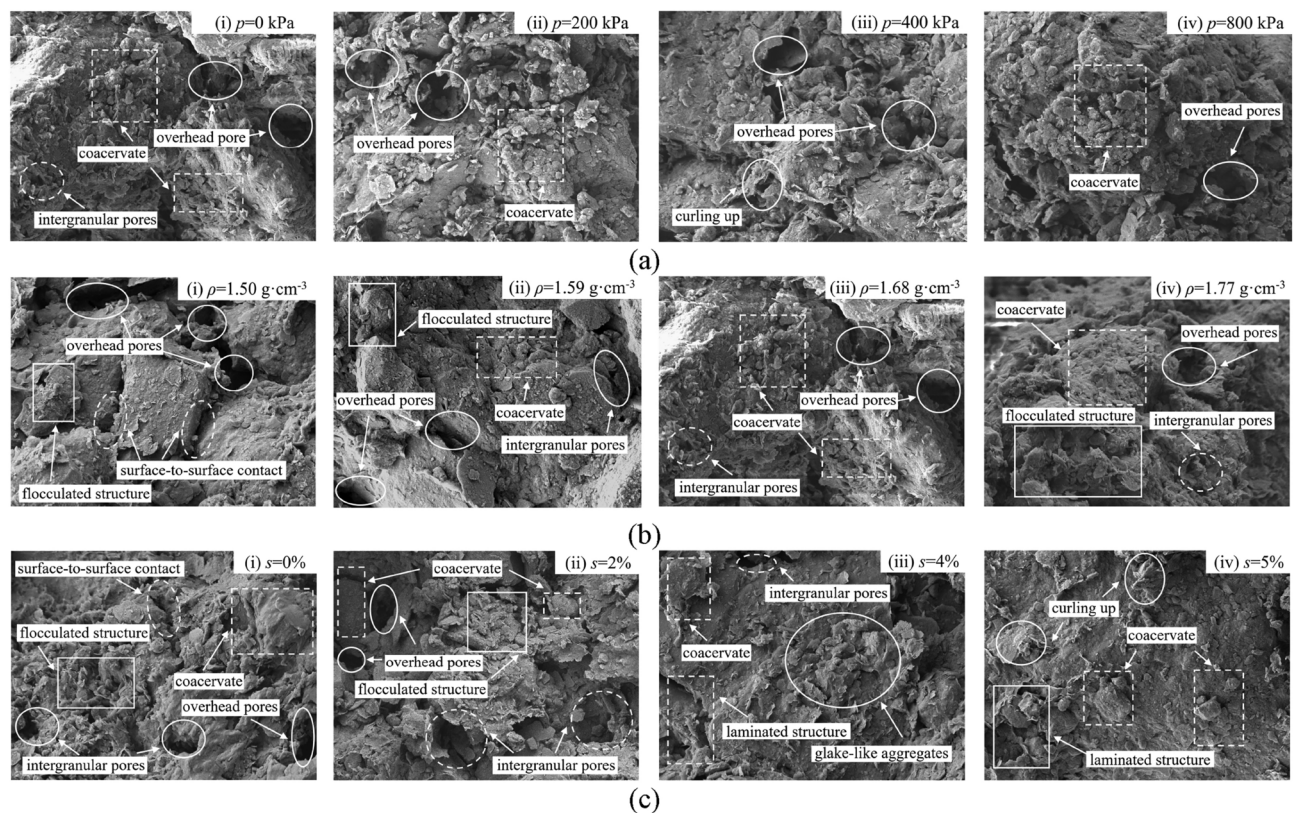

Fig. 9. 4000 × scanning electron microscopy images: (**a**) different consolidation pressures; (**b**) different dry densities; (**c**) different salt contents.

consisting of fine clay particles arranged in laminated and flat formations. Some aggregates resemble wave-like or flower-like structures, contributing to a turbulent structure similar to water flow. With increasing consolidation pressure, the particles appear more flattened, and the phenomenon of aggregation becomes more pronounced. The lamellar particles align in parallel, creating a highly oriented laminar flow structure. Consequently, the flocculation structure transitions into a combined turbulent and laminar flow structure, and the compression curve visibly shifts from gentle to steep. (2) Figure 9b shows SEM images of the samples at different dry densities. The image indicates that at a ρ_d of 1.50 g·cm^{-3}, the soil structure is notably loose, characterized by numerous

pores among the particles and a clear flocculation structure. The structural units mainly interact in a face-to-face manner. As the dry density increased, both the flocculation structures and the aggregates within the sample increased in abundance. Concurrently, the pores between the particles decrease significantly, explaining why the compression coefficient decreases as the dry density increases. (3) Figure 9c shows SEM images of the samples with varying salt contents. The image shows that at 0% salt content, the soil structure is relatively loose, with minimal aggregates and predominantly face-to-face particle contacts. When the salt content is less than 2%, the number of aggregates and pores between particles increase, and the contacts between particles change from face-to-face to point-to-face, with pronounced overhanging pores. This increase in porosity leads to an increase in the compression coefficient. Conversely, when the salt content exceeds 2%, the increase in salt leads to more rough and irregular aggregates on the soil surface, which also becomes more voluminous. The lamellar structure becomes more distinct, and the particles are tightly arranged, resulting in a decrease in the compression coefficient on a macroscopic scale.

Figure 10 shows the changes in the micro-parameters of the initial sample with different consolidation pressures, dry densities, and salt contents. Among them:

(1) Pore size and distribution: According to Zhang et al.[32], clay pores are classified into macropores (d > 10 μm), mesopores (1 < d < 10 μm), micropores (0.1 < d < 1 μm), and nanopores (d < 0.1 μm). Figure 10a shows curves of the changes in pore quantity and size distribution under the different consolidation pressures. Figure 10a shows that the total number of pores decreases gradually with increasing consolidation pressure, and the number of large and medium pores decreases significantly. Although there are fluctuations in the number of medium-sized and microscopic pores, the changes in the number of these pores are small. With increasing consolidation pressure, the proportion of large and medium pores in the sample decreases gradually, and V_{3D} is negatively correlated with the consolidation pressure in an exponential manner. Figure 10b shows the curves of pore quantity and size distribution changes under different dry densities and salt contents. Figure 10b shows that the total number of particles decreases progressively as the dry density increases, with the dry density showing a positive linear correlation with the three-dimensional porosity (V_{3D}). The changes in particle number and V_{3D} occur in two phases, with $s = 2\%$ serving as the critical turning point. At $s = 2\%$, both the lowest particle count and the peak V_{3D} are observed.

(2) Morphological characteristics: Fig. 10c shows the distribution of the abundance and frequency of round-ness distributions of the samples under the different consolidation pressures. As shown in Fig. 10c, the abundance is generally stable under the different consolidation pressures, ranging from 0.4–0.5 to 0.9–1.0, with the largest proportion ranging from 0.4 to 0.5, and the abundance changes little in the other intervals. As a result of the change in particle roundness, VR (extremely rounded) accounts for 67.63%–73.85% of the total and gradually decreases with increasing consolidation pressure, and the overall distribution of the particles tends toward A (angular) and SA (subangular). Figure 10d shows the distribution of the abundance values of samples with different dry densities and salt contents. As shown in Fig. 10d, the abundance values are concentrated at 0.4–0.5, 0.6–0.7 and 0.9–1.0 for the different dry densities and salt contents. With increasing dry density, there was no significant change in abundance at other intervals. With increasing salt content, the average abundance changed the most at $s = 2\%$.

(3) Arrangement characteristics: Fig. 10e shows the directional frequency distributions of sample particles under various consolidation pressures. The particle angles predominantly range between 0 to 15° and 75 to 90°, indicating distinct directional characteristics. Moreover, the proportion is maximal when the consolidation pressure is low in other intervals. Figure 10f presents the directional frequency distributions of sample particles with different dry densities and salt contents. With increasing dry density, the particle arrangement tends toward greater randomness, resulting in a more uniform distribution. With respect to varying salt contents, the distribution of the particle direction frequency exhibits two prominent peaks and approximates a right angle. Notably, the proportion of particles in the vertical direction constitutes 30.1% of the polar angle range, with the angle of the particle directional frequency distribution gradually increasing with increasing salt content.

Effects of microstructural features on compressibility
The Pearson correlation coefficient is used to assess how parameters such as pore number, V_{3D}, average particle abundance, and average particle directional frequency impact the compression coefficient and compression index. Table 5 displays the correlations between a_v, C_c, and micro-parameters across different dry densities and salt contents. According to Table 5, the pore number and V_{3D} exhibit the strongest correlations with a_v and C_c at various dry densities, with correlation coefficients exceeding 0.94 in absolute value. With respect to the salt content, V_{3D} had the highest correlation with a_v and C_c. Figure 11 presents the relationship curves between a_v, C_c, and the micro-parameters. As depicted in Fig. 11, under the influence of dry density, a_v and C_c have linear negative and positive correlations with the total pore number and V_{3D}, respectively. Conversely, under the influence of the salt content, both a_v and C_c increase as V_{3D} increases.

Penetration test
Analysis of macro results
Figure 12 shows the variation curves of the saturated permeability coefficients of saline clay across different dry densities and salt contents. (1) Figure 12a shows the relationship curve between the saturated permeability coefficient and dry density. Figure 12a clearly shows that dry density significantly influences the saturated permeability coefficient k_{s1}, which decreases exponentially until it stabilizes. (2) Figure 12b shows the relationship between the salt content and the saturated permeability coefficient. As shown in Fig. 12b, the saturated permeability coefficient k_{s2} of saline clay with various salt contents predominantly ranges from 5×10^{-6}
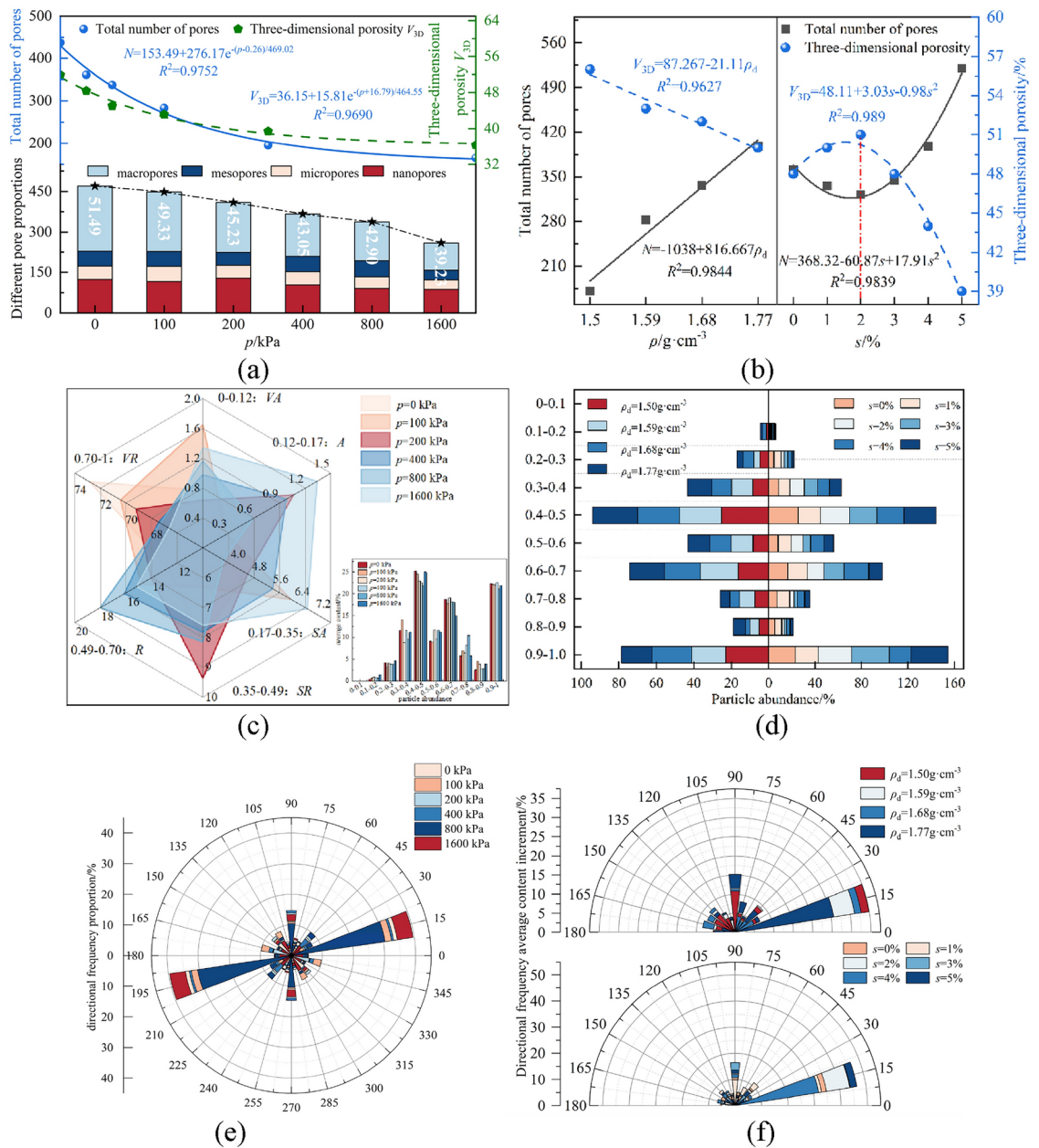
Fig. 10. $4000\times$ SEM images of initial samples under different dry densities and salt contents: (**a**) changes in the number and size distribution of pores under different consolidation pressures; (**b**) changes in the number and size distribution of pores under different dry densities and salt contents; (**c**) distribution of abundance values and roundness distribution frequency of samples under different consolidation pressures; (**d**) distribution of abundance values of samples under different dry densities and salt contents; (**e**) directional frequency distribution of sample particles at different consolidation pressures; (**f**) directional frequency distribution of sample particles under different dry densities and salt contents.

to 2.5×10^{-5} cm·s^{-1}. The increasing trend of the saturated permeability coefficient k_{s2} of samples with salt contents of 2% and less is not obvious with increasing salt content. The value of k_{s2} starts to decline sharply from $s=2\%$ with increasing salt content.

Microscopic analysis of results
SEM images of samples with varying dry densities and salt concentrations following permeation were obtained via microscopic examination at 10,000× magnification. Figure 13 shows the microstructures of cohesive soils with various dry densities and salt concentrations after permeation. (1) Figure 13a shows the microstructures of the samples with different dry densities following permeation. Figure 13a shows that at lower dry densities, the particles appear swollen due to percolation, and the structure is predominantly flocculated with a supportive
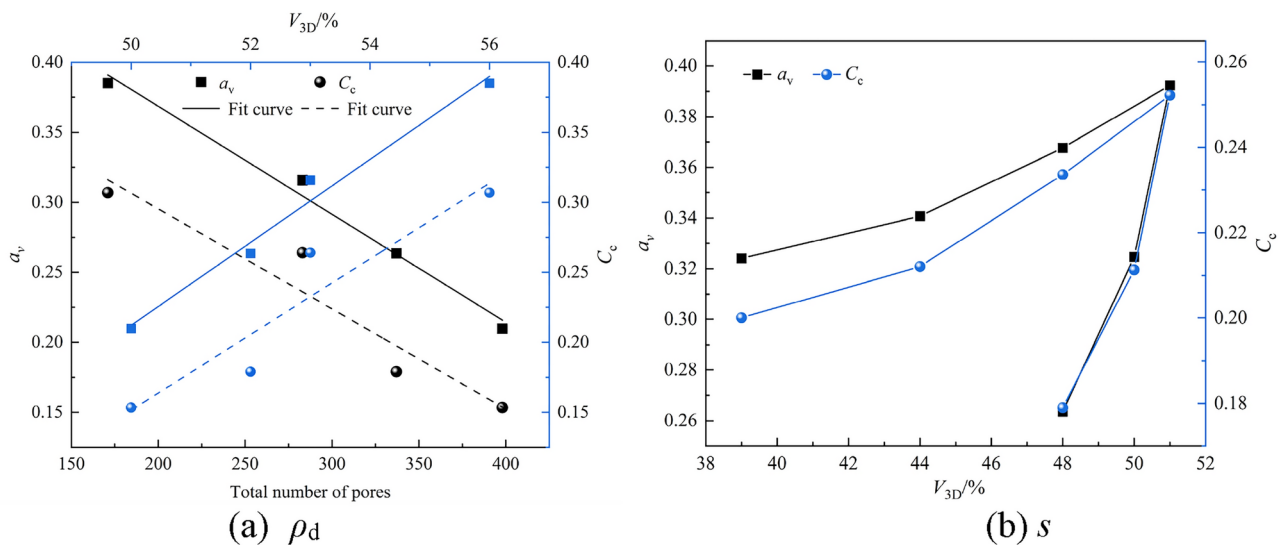
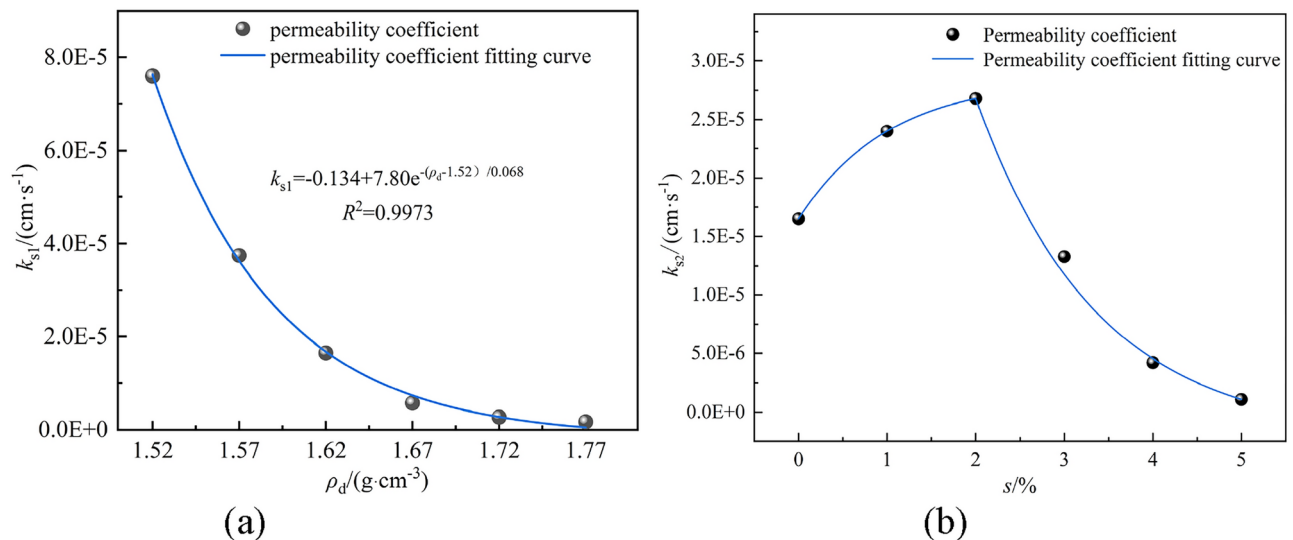**Fig. 11**. a_v and C_c are related to the microscopic parameters.

Fig. 12. Variation curves of the permeability coefficient with different factors: (**a**) variation in the permeability coefficient with different dry densities; (**b**) variation in the permeability coefficient with different salt contents.

turbulent structure. Numerous overhead pores are present between the soil masses, where the impediment of particle migration by the percolation pores is the predominant effect. There are few enclosed pores formed by flocculation, yet the connectivity of the pores is effective. With increasing dry density, the larger particle aggregates break apart, and the finer particles fill into the larger pores, reorganizing due to water film adsorption. The number of large pores decreases, the pore connectivity worsens, and the saturated permeability coefficient decreases. (2) Figure 13b shows the microstructures of the samples with varying salt concentrations after permeation. As noted in Fig. 13b, with salt concentrations below 2%, the introduction of salt as an electrolyte causes an increase in the ionic presence in the sample, enhancing ion adsorption and exchange. This leads to the agglomeration of some finer particles, identified as clay particles, from the particle size test results. Concurrently, salt addition increases electrostatic attraction among particles, promoting flocculation, which reduces the number of large overhead pores and increases the number of interparticle pores. When the salt concentration exceeds 2%, the number of coarse and irregular aggregates on the soil surface increases, as does their volume, indicating that salt contributes to a roughening effect on soil particles, forming sheet-like and layered structures. Upon reaching a salt concentration of 5%, extensive salt crystals precipitate on the sample surface, and the permeability coefficient initially increases but then decreases, with a turning point at $s = 2\%$.

Figure 14 shows the variations in the microscopic parameters at different dry densities and salinity levels following infiltration. (1) Figure 14a–c show the variation curves for the number and size distribution of pores,
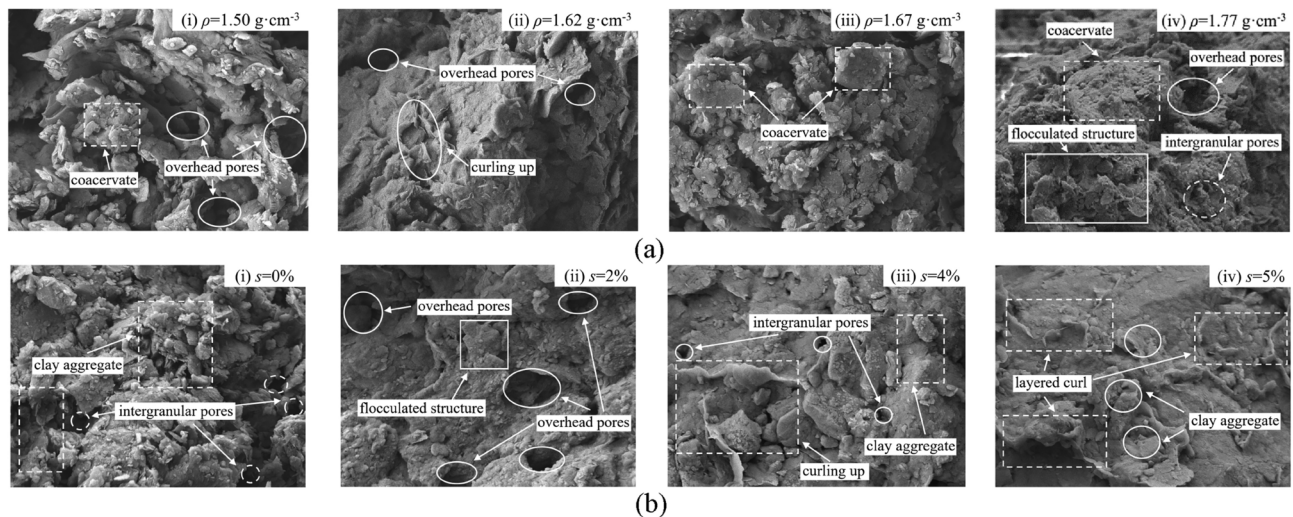
Fig. 13. 10,000×SEM images after infiltration: (**a**) different dry densities after infiltration; (**b**) different salt contents after infiltration.

the changes in particle morphological characteristics, and the frequency of pore orientation under varying dry densities after infiltration. Figure 14a–c clearly show that with increasing dry density, the number and proportion of large pores decrease progressively, whereas the number of micro- and nanopores fluctuates, but their proportion increases gradually. The total pore count also decreases linearly as the dry density increases. The V_{3D} is exponentially negatively correlated with dry density, as evidenced by an R^2 value of 0.9961. The abundance values are primarily concentrated between 0.4 and 0.5 and between 0.9 and 1.0. With increasing dry density, the particle morphology post-infiltration tends toward angular and polar angular shapes. A comparison of particle distribution diagrams under different dry densities post-infiltration reveals changes in the abundance of particle units due to increased dry density. The percentage of abundance values between 0.9 and 1 gradually decreases with increasing dry density, whereas the other ranges change little. Compared with the above results, after infiltration, the particle morphology generally shifts to a polar circular shape. (2) Figure 14d–f show the variation curves of pore number and size distribution, the change in particle morphological characteristics, and the change in pore orientation frequency under different salinities after infiltration. Figure 14d–f show that as the salinity increases, with s = 2% as the turning point, the proportion of large pores first increases and then decreases, and s = 2% is the maximum point. The nanopores exhibit the opposite trend, with s = 2% being the lowest point. The total number of pores and V_{3D} both show a two-stage change, which first increases linearly and then decreases linearly. The R^2 values are both greater than 0.88. Overall, the abundance values under the different salinities were relatively stable and were mainly concentrated at 0.4–0.5, 0.6–0.7 and 0.9–1.0, and there was no significant change in the abundance values in the other ranges. According to the statistics, the roundness of the particle aggregates under each salinity treatment slightly changed with increasing salinity. The proportion of polar roundness clearly reaches the upper limit when s = 2%. The directional distribution of sample pores is obvious and is concentrated from 0 to 15°, and the proportion decreases first and then increases with increasing salinity. When s = 2%, it is the lowest value.

Influence of microstructure characteristics on permeability parameters
Pearson correlation analysis was employed to assess the relationships among the macro-, meso-, micro-, and nanopores proportions; V_{3D}; average particle roundness; average particle abundance; average particle orientation frequency; and saturated permeability coefficient (k_s). Table 6 presents the correlations between the saturated permeability coefficient and the micro-parameters. According to Table 6, the proportion of micropores and V_{3D} exert the most significant influence on the permeability coefficient (k_{s1}) under varying dry densities. Specifically, the proportion of nanopores has a linear negative correlation with k_{s1}, whereas V_{3D} has a linear positive correlation with k_{s1}. Conversely, the total pore count and proportion of nanopores exert the most substantial impact on the permeability coefficient (k_{s2}) under different salt concentrations. Notably, the proportion of nanopores displays a linear negative correlation with k_{s2}, whereas the total pore count demonstrates a linear positive correlation with k_{s2}, as depicted in Fig. 15.

The empirical formula for fitting the permeability coefficient with the micro-parameters is as follows:
Dry density:

$$k_{s1} = 1.36 - 1.48 \times 10^{-5} P_s \tag{3}$$

$$k_{s1} = -1.58 + 3.34 \times 10^{-6} V_{3D} \tag{4}$$
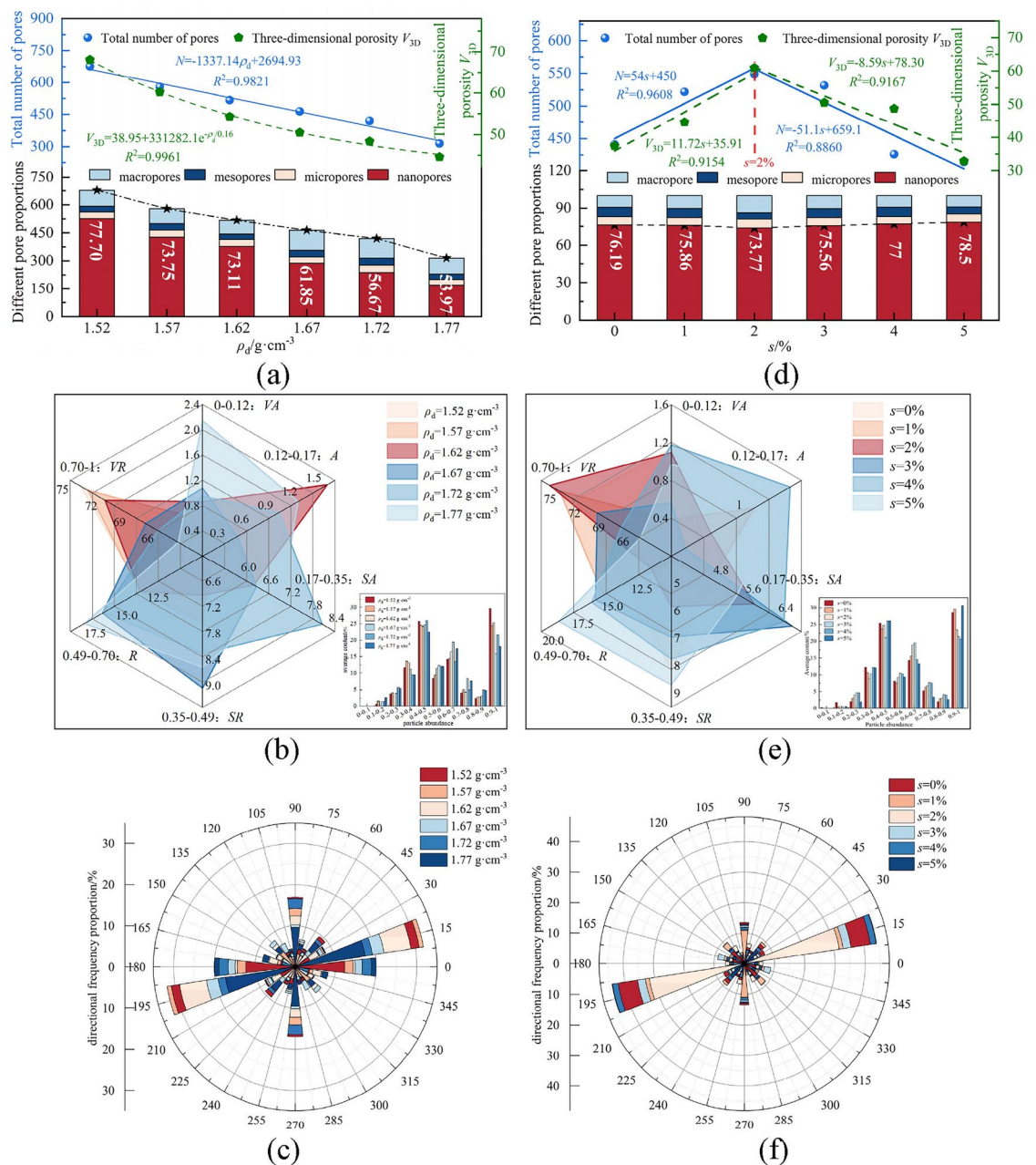
Different salinities:

Fig. 14. Changes in microscopic parameters after infiltration under different conditions: (**a**) pore size and distribution under different dry densities after penetration; (**b**) morphological characteristics of particles under different dry densities after penetration; (**c**) directional distribution frequency of particles under different dry densities after penetration; (**d**) pore size and distribution under different salt contents after infiltration; (**e**) morphological characteristics of particles under different salt contents after penetration; (**f**) directional distribution frequency of particles under different salt contents after penetration.

Correlation	Total number of pores	Macro-pores	Mesopores	Micro-pores	Nanopores	V_{3D}	Average particle roundness	Average particle abundance	Orientation frequency
k_{s1}	0.803*	− 0.798	− 0.836*	− 0.850*	− 0.827*	0.966**	0.842*	0.830*	− 0.784
k_{s2}	0.823*	0.748	− 0.147	0.538	− 0.882*	0.573	0.067	0.262	− 0.128

Table 6. Correlations between the permeability coefficient and microscopic parameters.
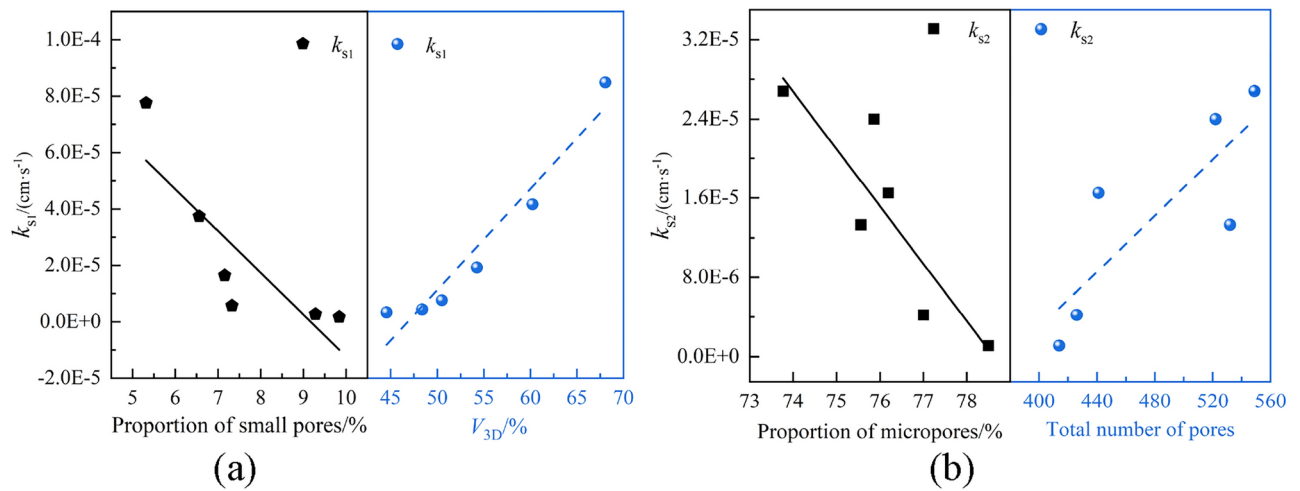
Fig. 15. Correlations between the saturated permeability coefficient and microscopic parameters under different conditions: (**a**) different dry densities and (**b**) different salt contents.

$$k_{s2} = 4.55 - 5.79 P_{\mathrm{mic}} \tag{5}$$

$$k_{s2} = -5.37 + 1.4N \tag{6}$$

where P_s, P_{mic}, and N represent the proportions of micropores, nanopores, and total pores, respectively.

Model prediction
SVR model
The support vector machine (SVM) is a supervised learning method rooted in statistical learning theory and was initially introduced by Vapnik in 1995. Over time, SVMs have been widely applied in addressing small-sample pattern classification (SVC) and nonlinear regression (SVR) tasks. Its core principle involves mapping input data to a higher-dimensional space via a kernel function, thereby addressing nonlinear regression challenges within a lower-dimensional space. Support vector regression (SVR) is classified as a black-box modeling approach that establishes the connection between input and output on the basis of available sample data. Given a training sample $S = \{(x_i, y_i \,| i = 1, 2, \cdots, l)\}, x_i, y_i \in R$, a regression function is constructed[33]:

$$f(x) = \omega' \varphi'(x) + b \tag{7}$$

where $f(x)$ is the output function, ω' is the weight vector, and $\varphi'(x)$ is the nonlinear mapping function. To promote effective sparsity in SVR, the insensitive loss function ε is introduced, transforming the problem into a convex optimization challenge:

$$\min \frac{1}{2} \|\omega\|^2 \tag{8}$$

Constraint conditions:

$$\begin{cases} y_i - \omega' x_i - b \leq \varepsilon \\ \omega' x_i + b - y_i \leq \varepsilon \end{cases} \tag{9}$$

Considering the allowed fitting error, the slack variables $\xi_i \geq 0$ and $\xi_i^* \geq 0$ are introduced so that SVR is transformed into the minimization problem of the following objective function:

$$\min \frac{1}{2} \|\omega\|^2 + C \sum_{i}^{l} (\xi_i^j \geq \xi_i^{j*}) \tag{10}$$

$$s.t. \begin{cases} y_i - \omega' x_i - b \leq \varepsilon + \xi_i \\ \omega' x_i + b - y_i \leq \varepsilon + \xi_i^* \\ \xi_i, \xi_i^* \geq 0 \end{cases} \tag{11}$$

Equation (12) is converted into a quadratic programming problem via the duality principle, and the Lagrange equation is established[34]:

$$l(\omega', \xi_i, \xi_i^*) = \frac{1}{2}(\omega' \cdot \omega') + C \sum_{i}^{l} (\xi_i^j \geq \xi_i^{j*}) - \sum_{i=1}^{l} \alpha_i(\varepsilon + \xi_i - y_i + \omega' x_i + b)$$
$$- \sum_{i=1}^{l} \alpha_i^*(\varepsilon + \xi_i^* - y_i + \omega' x_i + b) - \sum_{i=1}^{l} (\beta_i \xi_i + \beta_i^* \xi_i^*)$$

(12)

where $l(\omega', \xi_i, \xi_i^*)$ is the dual form of the Lagrange equation, and α_i, α_i^*, β_i, and β_i^* are the Lagrange operators. The partial derivatives of parameters ω', b, ξ_i, and ξ_i^* in the above formula should all be equal to zero. When this condition is substituted into the formula, the dual optimization problem is obtained:

$$\min \frac{1}{2} \sum_{i,j=1}^{l} (\alpha_i - \alpha_j^*)(\alpha_j - \alpha_j^*) [\varphi(x_i) \cdot \varphi(x_j)] + \sum_{i=1}^{l} \alpha_i(\varepsilon - y_i) + \sum_{i=1}^{l} \alpha_i^*(\varepsilon - y_i)$$

(13)

$$s.t. \begin{cases} \sum_{i=1}^{l} (\alpha_i - \alpha_i^*) = 0 \\ \alpha_i, \alpha_i^* \in [0, C] \end{cases}$$

(14)

In the formula, $\varphi(x_i) \cdot \varphi(x_j)$ represents the dot product operation in high-dimensional space. Let $K(x_i, y_i) = \varphi(x_i) \cdot \varphi(x_j)$, and $K(x_i, y_i)$ is called the kernel function, which is used to solve the dimension problem. Finally, the regression function is obtained as:

$$f(x) = \sum_{i=1}^{l} (\alpha_i - \alpha_i^*) K(x_i, y_i) + b$$

(15)

The kernel function $K(\cdot)$ must adhere to Mercer's theorem and fulfill the requirements of the inner product algorithm. Commonly used kernel functions include the linear kernel function, Gaussian radial basis function (RBF) kernel function, polynomial kernel function, and sigmoid kernel function. This study opts for the RBF kernel function because of its robust non-linearity and relatively low computational complexity. Its formulation is as follows:

$$K(x, y) = \exp - \left(\frac{1}{2p} \| x - y \|^2 \right)$$

(16)

As evident from formulas (8) and (14), the prediction efficacy of SVR is significantly influenced by the kernel function parameter p and the penalty factor C. Inappropriate parameter settings can substantially decrease the predictive accuracy of SVR. Hence, it becomes imperative to devise a suitable approach for globally optimizing hyperparameters to enhance their prediction performance.

Improved PSO algorithm
PSO algorithm
PSO is a global optimization algorithm that emulates the cooperative behavior observed in bird flocks during foraging. Renowned for its simplicity and rapid convergence, PSO has been extensively applied in parameter optimization tasks. The algorithm commences with the initialization of a cluster of random particles, which then iteratively seek the optimal solution. Throughout the iteration, the particles update their positions primarily on the basis of individual extreme values (individual experience) and collective extreme values (population experience). Additionally, particles facilitate information exchange by tracking these two extreme values[35].

Suppose that the swarm comprises M particles and that each particle possesses D-dimensional vectors that represent its position and velocity. After initialization, the particles exhibit the following attributes:

where $X_i = (x_{i1}, x_{i2}, \cdots, x_{iD})$ represents the position of the i-th particle and where $P_i = (p_{i1}, p_{i2}, \cdots, p_{iD})$ signifies the best position visited by the i-th particle, which is also known as p_{best}. The best individual among all $P_i(i = 1, \cdots, N)$ is recognized as the best position g_{best} ever attained by the entire particle swarm $V_i = (v_{i1}, v_{i2}, \cdots, v_{iD})$, which represents the flight velocity of the i-th particle. The formula for updating the position of each particle is as follows:

$$v_{id}(t+1) = w' \times v_{id}(t) + c_1 \times r_1(p_{best} - p) + c_2 \times r_2(g_{best} - p)$$

(17)

$$x_{id}(t+1) = x_{id}(t) + v_{id}(t+1)$$

(18)

In the formula, d represents the current number of iterations, w' represents the inertia coefficient, regulating the balance between global and local search; c_1 represents the cognitive constant, facilitating self-awareness, typically set to 2; c_2 represents the social constant, mimicking interaction with the social population, also set to

2; and r_1 and R^2 represent random numbers uniformly distributed in the interval [0,1] and are utilized to prevent local optima.

Improved PSO algorithm
Formula (17) clearly shows that as w' increases, the PSO algorithm's global search capability strengthens; conversely, as w' decreases, its local search capability strengthens. To maintain a balance between the global and local optimization abilities of the particle swarm optimization algorithm and ensure swarm stability, the enhanced PSO algorithm adjusts the inertia weight. This adjustment facilitates robust global search capability in the initial stages, gradually enhancing local search capability as the iteration count increases. The modified weight formula is presented below:

$$w^d = w_{start} - (w_{start} - w_{end})(\frac{d}{K})$$
(19)

In the formula, d represents the current iteration count, K denotes the total number of iterations, w_{start} is typically set to 0.9, and w_{end} is typically set to 0.4.

Improved PSO-SVR mechanical property index prediction model

As previously noted, the hyperparameters of the SVR model, including the kernel function parameter p and the penalty factor C, significantly influence the model's accuracy. In particular, the penalty coefficient C primarily impacts the model's robustness in prediction. A smaller value implies a lower penalty on empirical errors, potentially leading to increased training errors, whereas a larger value may result in a reduced generalization ability of the SVR model. The width parameter p of the RBF kernel function predominantly influences the complexity of the distribution in the high-dimensional feature space. Inappropriate values of p can lead to overfitting or underfitting phenomena. This study introduces an enhanced PSO method to optimize the selection of these two hyperparameters, consequently enhancing the accuracy of the prediction model. The detailed process of the improved PSO-SVR model is illustrated in Fig. 16.

Algorithm test analysis

The mechanical characteristics of saline clay result from various influencing factors. Considering these factors and their internal connections, key parameters, such as dry density, moisture content, and salt content, were identified to predict the mechanical and permeability properties of the soil. This study conducted 14 sets of direct shear and compression tests, with 10 sets randomly selected as training samples and the remaining 4 as test samples. For the permeability tests, 12 sets of data were analyzed, with 8 sets chosen randomly as training samples and the last 4 as test samples. An SVM prediction model was developed using the same data, and its results were compared with those of the improved PSO-SVR, as depicted in Fig. 17. Figure 17 clearly shows that the prediction accuracy of the improved PSO-SVR model surpasses that of the SVM model.
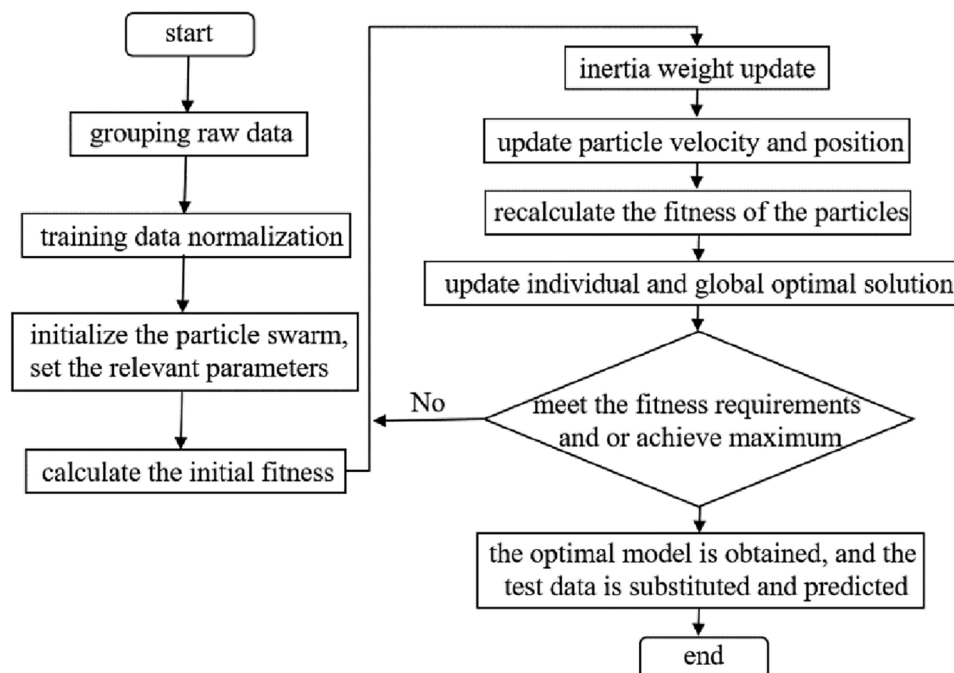

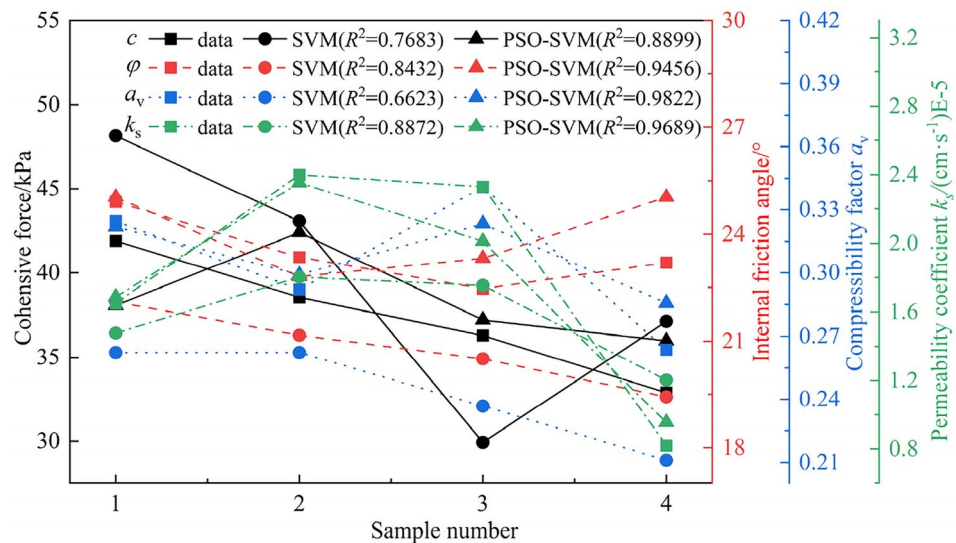**Fig. 16**. Improving the PSO-SVR algorithm process.

Fig. 17. Comparison of predictions between the SVR and improved POS-SVR models.

Discussion

Previous studies have indicated that the strength of saline clay decreases as the water content increases[36,37] and increases with increasing dry density and salt content. The effect of salt content on soil strength is due to salt expansion and pore plugging[38].

The addition of Na_2SO_4 increases the ion concentration in pore water and enhances the electromotive force potential, causing the dispersion of cementation and a reduction in cohesion. With a further increase in Na_2SO_4, the cementation by salt crystals between particles begins to replace the accumulation contacts between them, and these crystals fill the soil pores, thereby increasing cohesion. Minimal addition of Na_2SO_4 results in a looser arrangement of the particle framework and a decrease in cohesion. As the amount of Na_2SO_4 increases, cementation by salt crystals increases, the soil framework becomes more compact, and the internal friction angle increases progressively. Moreover, the strength of the soil varies abruptly at a salt content of 2%. A schematic diagram illustrates the macro–micro mechanism of this sudden change at $s = 2\%$ (Fig. 18). As shown in Fig. 18, the introduction of a small quantity of salt reduces the thickness of the water film between clay particles[39], enhancing the flocculation effect in the soil[40,41]. With a limited and discontinuous flocculation capacity, overhead pores become pronounced. However, as the salt content increases further, salt crystals start to occlude pores, progressively increasing the soil strength[42].

In summary, the interaction between soluble salt and pore water in saline clay alters the microstructure of the soil, impacting its strength and permeability. Current studies indicate that concentrations of soluble salts (NaCl, KCl, $CaCl_2$, and $NaHCO_3$) ranging from 0 to 2% do not significantly affect clay strength. However, the saline clay analyzed in this research, sourced from the arid region of northern China, contains high levels of soluble salts, with sulfate ion concentrations reaching 0.568%. The clay content is high, and salt ions readily adsorb and bind with clay particles to form aggregates, with $s = 2\%$ identified as the critical point for changes in soil strength.

When constructing water diversion projects in such arid regions of China, where soil masses consist of relatively large particles and are in the transition stage of silt–clay, careful monitoring of these sudden strength changes is essential. Nonetheless, this paper primarily addresses the impact of a single factor on the mechanical properties of cohesive soil, neglecting the salt-frost heaving and thaw settlement characteristics of saline soil due to temperature variations, as well as the interplay among various factors. In real-world engineering disasters, the effects of ambient temperature changes are often significant. Consequently, further research is planned to explore the impact of multifactorial interactions on the strength characteristics of saline soil under temperature variations. This study uses existing experimental data to enhance the PSO-SVR prediction model and utilizes existing research data for validation. However, this research only compares the SVM and PSO-SVR prediction models. There remains a need to explore simpler and more rapid prediction models for assessing soil strength.

Conclusions

Through indoor direct shear, compression, permeation, and scanning electron microscopy tests conducted on saline clay from the arid region of northern China, this study investigated the impacts of varying water contents, dry densities, and salt contents on the mechanical properties of clay. The key findings are summarized as follows:

(1) With increasing dry density, the particles become denser, the effective contact area increases, and the co-hesion and internal friction angle increase. With increasing water content, the pore water decreases, the ice cementation effect weakens, the matric suction between soil particles decreases, and the cohesion and in-ternal friction angle gradually decrease. When the salt content decreases, the shear strength decreases with increasing salt content. At a salt content of 2%, the soil pore water saturates, causing excess salt to crystallize
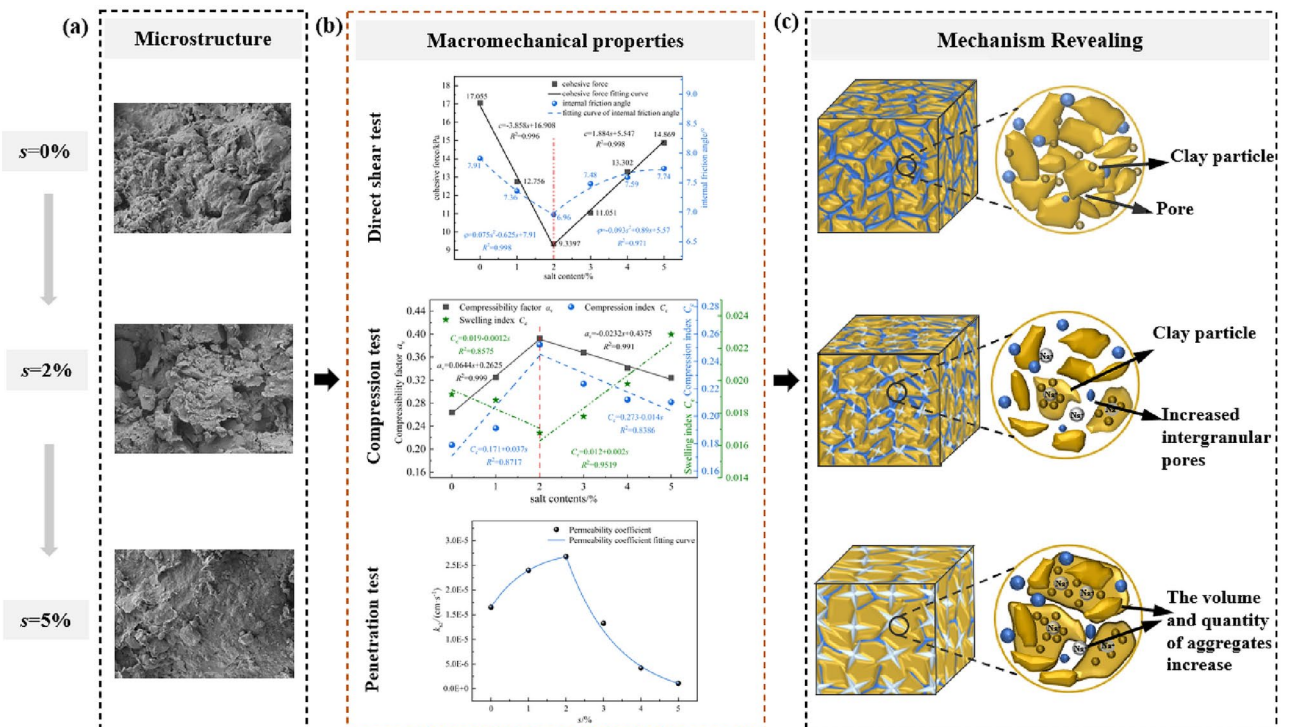
Fig. 18. Macro micro-mechanism of different salt contents: (**a**) SEM images of microstructural changes in soil under different salt contents; (**b**) changes in the macroscopic mechanical properties of samples with different salt contents; (**c**) schematic diagram of the influence of different salt contents on the microstructure mechanism of the soil.

within the soil layer. This crystallized salt acts as a cementation agent, enhancing cohesion and increasing the internal friction angle.

(2) Compression characteristics: With increasing water content, the initial porosity ratio remains stable, whereas the compression coefficient increases, and both the compression index and resilience coefficient gradually decrease. An increasing dry density leads to a decrease in the initial porosity ratio, compression coefficient, compression index, and resilience coefficient. The salt content changes the initial porosity ratio, but the compression coefficient and compression index initially increase but then decrease. Moreover, the resilience coefficient initially increases, then decreases, and finally increases again, with $s = 2\%$ marking the critical point. Scanning electron microscopy revealed that as the consolidation pressure increased, the soil structure type gradually evolved from a flocculent structure to a turbulent and laminar flow structure, with an obvious particle aggregation effect, and the compression coefficient of the saline soil decreased. Through correlation analysis, the compression coefficient and compression index are strongly correlated with the three-dimensional porosity.

(3) Permeability characteristics: With increasing dry density, the saturated permeability coefficient of saline clay decreases. With increasing salt content, the saturated permeability coefficient first increases but then decreases. The electron microscopy results revealed that with increasing dry density, the number of large particle aggregates decreased, and the number of small particles increased. The sample structure progressively densified, reducing the porosity ratio and increasing the water flow resistance, resulting in a gradual decrease in the saturated permeability coefficient, with the declining trend slowing. At $s < 2\%$, ion adsorption and exchange led to a reduction in the number of overhead macropores, an increase in interparticle porosity, and an increase in seepage channels. However, with increasing salt content, the internal pores of the soil become filled with precipitated salt crystals, blocking seepage channels and thereby reducing the saturated permeability coefficient. Correlation analysis revealed that three-dimensional porosity had the greatest influence on the saturated permeability coefficient of saline soil.

(4) Prediction and validation of the strength and permeability characteristics involved the selection of three experimental parameters: water content, dry density, and salt content. A comparison between the SVM and PSO-SVR prediction results indicated superior accuracy and broader applicability for the latter. Verification with independent data demonstrated its suitability for predicting the strength and permeability characteristics of saline clay, offering a relatively fast and accurate method for onsite assessment.

Data availability

The datasets used and/or analysed during the current study available from the corresponding author on reasonable request.

References

1. Niu, X. & Gao, J. Establishment of volume change relationship of sulfate saline soil considering salt heaving and frost heaving. *J. Geotech. Eng.* **37**(04), 755–760 (2015) (**in Chinese**).
2. Shimbo, T. et al. Effect of water contents and initial crack lengths on mechanical properties and failure modes of pre-cracked compacted clay under uniaxial compression. *Eng. Geol.* **301**, 106593. https://doi.org/10.1016/j.enggeo.2022.106593 (2022).
3. Sun, W. et al. Moisture tension in fine-grained reconstituted soils at high initial water contents. *Acta Geotech.* **15**, 2591–2598. https://doi.org/10.1007/s11440-020-00934-8 (2020).
4. Burland, J. B. On the compressibility and shear strength of natural clays. *Géotechnique* **40**(3), 329–378. https://doi.org/10.1680/geot.1990.40.3.329 (1990).
5. Kong, Z. et al. Experimental study on shear strength parameters of round gravel soils in plateau alluvial-lacustrine deposits and its application. *Sustainability* **15**(5), 3954. https://doi.org/10.3390/su15053954 (2023).
6. Zhu, H. et al. Mechanical characteristics of rice root-soil complex in rice-wheat rotation area. *Agriculture* **12**(7), 1045. https://doi.org/10.3390/agriculture12071045 (2022).
7. Xu, H. et al. Prediction of shear strength of fully weathered coastal red sandstone: Influence of water content, fine content, and relative compaction. *J. Coast. Res.* **37**(4), 827–841. https://doi.org/10.2112/JCOASTRES-D-20-00139.1 (2021).
8. Lan, T., Zhang, R., Yang, B. & Meng, X. Influence of swelling on shear strength of expansive soil and slope stability. *Front. Earth Sci.* **10**, 849046. https://doi.org/10.3389/feart.2022.849046 (2022).
9. Kang, Q. et al. Study on the effect of moisture content and dry density on shear strength of silty clay based on direct shear test. *Adv. Civ. Eng.* **2022**(1), 2213363. https://doi.org/10.1155/2022/2213363 (2022).
10. Guo, X. H., Wu, G. D. & Guo, X. H. Analysis of single factor on the low temperature compressive characteristics of sulphate saline soil. *Appl. Mech. Mater.* **501**, 426–429. https://doi.org/10.4028/www.scientific.net/AMM.501-504.426 (2014).
11. Butterfield, R. A natural compression law for soils (an advance on *e*-log*p'*). *Géotechnique* **29**(4), 469–480. https://doi.org/10.1680/geot.1979.29.4.469 (1979).
12. Kakihara, Y. et al. Shear strength-related properties of clayey soil mixed with converter steelmaking slag under overburden pressure for short-time curing. *Japan. Geotech. Soc. Spec. Publ.* **9**(6), 296–301. https://doi.org/10.3208/jgssp.v09.cpeg076 (2021).
13. Keller, T. et al. Analysis of soil compression curves from uniaxial confined compression tests. *Geoderma* **163**(1–2), 13–23. https://doi.org/10.1016/j.geoderma.2011.02.006 (2011).
14. Yamamoto, T. et al. Unconfined compressive strength of cement-stabilized soil cured under an overburden pressure. *Doboku Gakkai Ronbunshu* **2002**(701), 387–399. https://doi.org/10.2208/jscej.2002.701_387 (2002).
15. Wu, A. X., Yao, G. H. & Huang, M. Q. Influence factors of permeability during heap leaching of complex copper oxide ore. *Adv. Mater. Res.* **347**, 1037–1043. https://doi.org/10.4028/www.scientific.net/AMR.347-353.1037 (2012).
16. Zarooei, F. & Fereidooni, D. Assessing the effect of particle size distribution on permeability of silty-sandy soils. *Geotech. Geol. Eng.* **41**(6), 3681–3698. https://doi.org/10.1007/s10706-023-02481-x (2023).
17. Mawlood, Y. et al. Modeling and statistical evaluations of unconfined compressive strength and compression index of the clay soils at various ranges of liquid limit. *J. Test. Eval.* **50**(1), 551–569. https://doi.org/10.1520/JTE20200505 (2022).
18. Hu, Y. Correlation analysis of water content and dry density of red clay with shear strength[J]. *Yangtze River* **48**(S1), 249–252 (2017).
19. Kasha, A. et al. Integrated approach for closure correction of mercury injection capillary pressure measurements. *Geoenergy Sci. Eng.* **230**, 212245. https://doi.org/10.1016/j.geoen.2023.212245 (2023).
20. Smet, S. et al. Can the pore scale geometry explain soil sample scale hydrodynamic properties. *Front. Environ. Sci.* **6**, 20. https://doi.org/10.3389/fenvs.2018.00020 (2018).
21. Soares, M. V. T. et al. Pre-salt carbonate cyclicity and depositional environment: NMR petrophysics and Markov cyclicity of lacustrine acoustic facies (Santos Basin, Brazil). *Mar. Pet. Geol.* **157**, 106494. https://doi.org/10.1016/j.marpetgeo.2023.106494 (2023).
22. Feng, D. et al. Movable fluid evaluation of tight sandstone reservoirs in lacustrine delta front setting: Occurrence characteristics, multiple control factors, and prediction model. *Mar. Pet. Geol.* **155**, 106393. https://doi.org/10.1016/j.marpetgeo.2023.106393 (2023).
23. Yu, B. et al. Heterogeneous evolution of pore structure during loess collapse: Insights from X-ray micro-computed tomography. *Catena* **201**, 105206. https://doi.org/10.1016/j.catena.2021.105206 (2021).
24. Siddique, A. et al. Overcoming stereological Bias: A workflow for 3D mineral characterization of particles using X-ray micro-computed tomography. *Miner. Eng.* **201**, 108200. https://doi.org/10.1016/j.mineng.2023.108200 (2023).
25. Zhang, Y. et al. Evaluation of loess collapsibility based on random field theory in Xi'an, China. *Math. Probl. Eng.* **2022**(1), 8665061. https://doi.org/10.1155/2022/8665061 (2022).
26. Li, Z. et al. Mining and analysis of multiple association rules between the Xining loess collapsibility and physical parameters. *Sci. Rep.* **11**(1), 816. https://doi.org/10.1038/s41598-020-78702-7 (2021).
27. Motameni, S. et al. A comparative analysis of machine learning models for predicting loess collapse potential. *Geotech. Geol. Eng.* **42**(2), 881–894. https://doi.org/10.1007/s10706-023-02593-4 (2024).
28. Zhang, T. et al. GIS-based landslide susceptibility mapping using hybrid integration approaches of fractal dimension with index of entropy and support vector machine. *J. Mt. Sci.* **16**(6), 1275–1288. https://doi.org/10.1007/s11629-018-5337-z (2019).
29. Sanyal, S. et al. Designing injection water for enhancing oil recovery from kaolinite laden hydrocarbon reservoirs: A spectroscopic approach for understanding molecular level interaction during saline water flooding. *Energy Fuels* **31**(11), 11627–11639 (2017).
30. Sanyal, S. et al. Interaction study of clay-bearing amphibolite–crude oil–saline water: Molecular level implications for enhanced oil recovery during low saline water flooding. *J. Earth Syst. Sci.* **127**, 1–11 (2018).
31. Sanyal, S. et al. Interaction study of montmorillonite-crude oil-brine: Molecular-level implications on enhanced oil recovery during low saline water flooding from hydrocarbon reservoirs. *Fuel* **254**, 115725 (2019).
32. Zhang, X. et al. Evolution of microscopic pore of structured clay in compression process based on SEM and MIP test. *Chin. J. Rock Mech. Eng.* **31**(2), 406–412 (2012).
33. Haisheng, Li. *Research on Support Vector Machine Regression Algorithm and Application* (South China University of Technology, 2005).
34. Fukushi, D. et al. Scanning near-field optical/atomic force microscopy detection of fluorescence in situ hybridization signals beyond the optical limit. *Exp. Cell Res.* **289**(2), 237–244. https://doi.org/10.1016/s0014-4827(03)00259-3 (2003).
35. Eberhart R, Kennedy J. Particle swarm optimization[C]//Proceedings of the IEEE international conference on neural networks. 1995, 4: 1942–1948.
36. Dhanya, K. A., Venkatesh, T. S. D. & Divya, P. V. Influence of suction on the interface characteristics of unsaturated marginal lateritic soil backfills with composite geosynthetics. *Int. J. Geosynth. Ground Eng.* **9**(6), 73. https://doi.org/10.1007/s40891-023-00491-6 (2023).
37. Chen, C. et al. Shear strength characteristics of basalt fiber-reinforced loess. *Sci. Rep.* **13**(1), 15923. https://doi.org/10.1038/s41598-023-43238-z (2023).

38. Ma, D. et al. Dissolution load-settlement behaviour of saline soil and compression criterion for the natural foundation of high-speed railways. *Bull. Eng. Geol. Environ.* **81**(9), 366. https://doi.org/10.1007/s10064-022-02878-7 (2022).
39. Bojana, D. & Ludvik, T. The impact of structure on the undrained shear strength of cohesive soils. *Eng. Geol.* **92**(1/2), 88–96. https://doi.org/10.1016/j.enggeo.2007.04.003 (2007).
40. Bahloul, O., Abbeche, K. & Bahloul, A. Study of the microstructure of a collapsible soil flooded with NaCl saline[C]//E3S Web of Conferences. *EDP Sci.* **9**, 14001. https://doi.org/10.1051/e3sconf/20160914001 (2016).
41. Liu, J. et al. Study of constitutive models of reconstituted clay with high initial water content. *Sustainability* **15**(16), 12618. https://doi.org/10.3390/su151612618 (2023).
42. Wang, Y. et al. Study on the soil water characteristic curve and its fitting model of Ili loess with high level of soluble salts. *J. Hydrol.* **578**, 124067. https://doi.org/10.1016/j.jhydrol.2019.124067 (2019).

Acknowledgements

Author contributions

HC conceived the overall idea of the article and wrote the article. LZ conceived the overall idea of the article. CS contributed to the revision of the article. PF were responsible for the collection of relevant materials. All authors read and approved the final manuscript.

Funding

Declarations

Competing interests

The authors declare no competing interests.

Ethical approval

No conflict of interest exits in the submission of this manuscript, and manuscript is approved by all authors for publication. The work described was original research that has not been published previously. We declare that we do not have any commercial or associative interest that represents a conflict of interest in connection with the work submitted.

Additional information

Correspondence and requests for materials should be addressed to L.Z.

Reprints and permissions information is available at www.nature.com/reprints.

Publisher's note Springer Nature remains neutral with regard to jurisdictional claims in published maps and institutional affiliations.